

# Role of defects in ultra-high gain in fast planar tin gallium oxide UV-C photodetector by MBE

Cite as: Appl. Phys. Lett. **121**, 111105 (2022); <https://doi.org/10.1063/5.0107557>

Submitted: 05 July 2022 • Accepted: 22 August 2022 • Published Online: 16 September 2022

 Partha Mukhopadhyay,  Isa Hatipoglu,  Ymir K. Frodason, et al.



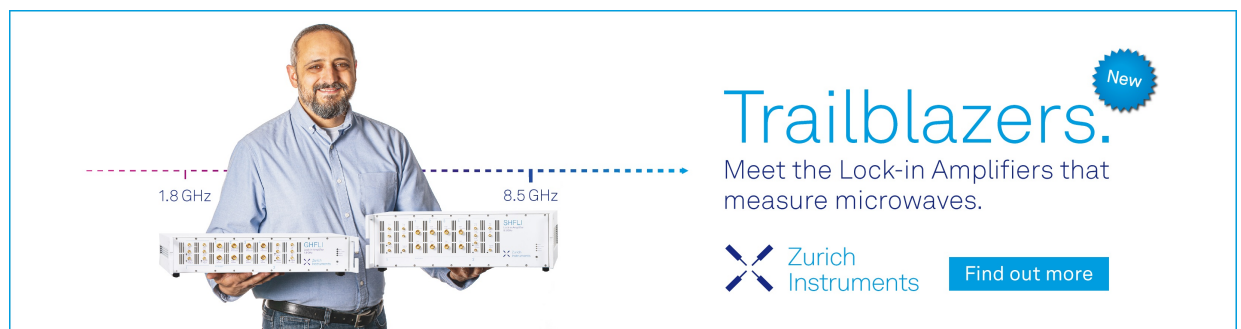
View Online




Export Citation




CrossMark



**Trailblazers.** 

Meet the Lock-in Amplifiers that measure microwaves.

 Zurich Instruments [Find out more](#)

# Role of defects in ultra-high gain in fast planar tin gallium oxide UV-C photodetector by MBE

Cite as: Appl. Phys. Lett. **121**, 111105 (2022); doi: [10.1063/5.0107557](https://doi.org/10.1063/5.0107557)

Submitted: 5 July 2022 · Accepted: 22 August 2022 ·

Published Online: 16 September 2022



View Online



Export Citation



CrossMark

Partha Mukhopadhyay,<sup>1,a)</sup> Isa Hatipoglu,<sup>2</sup> Ymir K. Frodason,<sup>3</sup> Joel B. Varley,<sup>4</sup> Martin S. Williams,<sup>5</sup> Daniel A. Hunter,<sup>5</sup> Naresh K. Gunasekar,<sup>6</sup> Paul R. Edwards,<sup>5</sup> Robert W. Martin,<sup>5</sup> Feng Wu,<sup>7</sup> Akhil Mauze,<sup>7</sup> James S. Speck,<sup>7</sup> and Winston V. Schoenfeld<sup>1,8,9,a)</sup>

## AFFILIATIONS

<sup>1</sup>CREOL, The College of Optics and Photonics, University of Central Florida, 4304 Scorpius St., Orlando, Florida 32816, USA

<sup>2</sup>Department of Electrical and Electronics Engineering, Şırnak University, Şırnak, Türkiye

<sup>3</sup>Department of Physics, Centre for Materials Science and Nanotechnology, University of Oslo, Oslo, Norway

<sup>4</sup>Lawrence Livermore National Laboratory, Livermore, California 94550, USA

<sup>5</sup>Department of Physics, SUPA, University of Strathclyde, Glasgow G4 0NG, United Kingdom

<sup>6</sup>School of Physics and Astronomy, Cardiff University, Cardiff CF24 3AA, United Kingdom

<sup>7</sup>Materials Department, University of California, Santa Barbara, California 93106-5050, USA

<sup>8</sup>Department of Electrical and Computer Engineering, University of Central Florida, Orlando, Florida 32816, USA

<sup>9</sup>Department of Materials Science and Engineering, University of Central Florida, Orlando, Florida 32816, USA

<sup>a)</sup>Authors to whom correspondence should be addressed: [partha.mukhopadhyay@creol.ucf.edu](mailto:partha.mukhopadhyay@creol.ucf.edu) and [winston@creol.ucf.edu](mailto:winston@creol.ucf.edu)

## ABSTRACT

We report ultra-high responsivity of epitaxial  $(\text{Sn}_x\text{Ga}_{1-x})_2\text{O}_3$  (TGO) Schottky UV-C photodetectors and experimentally identified the source of gain as deep-level defects, supported by first principles calculations. Epitaxial TGO films were grown by plasma-assisted molecular beam epitaxy on  $(-201)$  oriented n-type  $\beta\text{-Ga}_2\text{O}_3$  substrates. Fabricated vertical Schottky devices exhibited peak responsivities as high as  $3.5 \times 10^4$  A/W at  $-5$  V applied bias under 250 nm illumination with sharp cutoff shorter than 280 nm and fast rise/fall time in milliseconds order. Hyperspectral imaging cathodoluminescence (CL) spectra were examined to find the mid-bandgap defects, the source of this high gain. Irrespective of different tin mole fractions, the TGO epilayer exhibited extra CL peaks at the green band ( $\sim 2.20$  eV) not seen in  $\beta\text{-Ga}_2\text{O}_3$  along with enhancement of the blue emission-band ( $\sim 2.64$  eV) and suppression of the UV emission-band. Based on hybrid functional calculations of the optical emission expected for defects involving Sn in  $\beta\text{-Ga}_2\text{O}_3$ ,  $V_{\text{Ga}}\text{-Sn}$  complexes are proposed as potential defect origins of the observed green and blue emission-bands. Such complexes behave as acceptors that can efficiently trap photogenerated holes and are predicted to be predominantly responsible for the ultra-high photoconductive gain in the Sn-alloyed  $\text{Ga}_2\text{O}_3$  devices by means of thermionic emission and electron tunneling. Regenerating the  $V_{\text{Ga}}\text{-Sn}$  defect complexes by optimizing the growth techniques, we have demonstrated a planar Schottky UV-C photodetector of the highest peak responsivity.

Published under an exclusive license by AIP Publishing. <https://doi.org/10.1063/5.0107557>

Gallium oxide has become a natural choice for deep UV applications because of its ultra-wide optical bandgap that exceeds  $\sim 4.4$  eV at room temperature (RT).<sup>1</sup> Alloying  $\text{Ga}_2\text{O}_3$  with In,<sup>2</sup> Al,<sup>3</sup> and Sn<sup>4</sup> can modify the bandgap of the epilayer allowing UV-C optoelectronic devices to be tuned. Among them, tin gallium oxide photodetectors have become a viable path for ultra-high responsivity with shorter transient characteristics than its  $\text{Ga}_2\text{O}_3$  counterparts.<sup>4–6</sup> It has been a challenge to identify the source of high gains in  $\text{Ga}_2\text{O}_3$ -based photodetectors, and recent reports demonstrated its correlation with deep-level defects.<sup>6–9</sup> The fast progress of wide-bandgap metal-oxide relies

on the success in understanding and controlling their defects.<sup>10,11</sup> Cathodoluminescence (CL) hyperspectral imaging (HSI) becomes an invaluable tool for defect metrology because of its ability to map intensity variations or shifts in the emission wavelength.<sup>12</sup> Identifying the nature and the concentration of those defects in a material and further manipulating them to tune the functional properties in a desired manner have become an important part of defect engineering.<sup>13</sup>

In this research, we epitaxially grew TGO layers on  $(-201)$  Sn-doped  $\beta\text{-Ga}_2\text{O}_3$  substrates by plasma-assisted molecular beam epitaxy (PAMBE) and fabricated vertical Schottky solar-blind UV

photodetectors. Considering a planar device and heterojunctions with  $\text{Ga}_2\text{O}_3$ , the reported responsivity ( $3.5 \times 10^4$  A/W) in this paper is the highest for a UV-C Schottky photodetector.<sup>14</sup> We performed x-ray diffraction and cross-sectional high-resolution transmission electron microscopy (HRTEM) to investigate the crystalline quality of the film. An electron probe microanalyzer (EPMA) was used to measure room temperature CL (RTCL) as well as wavelength dispersive x-ray (WDX) spectroscopy to quantify the Sn composition. CL-HSI spectra were collected and analyzed to investigate optical emission related to deep-level defects.<sup>15</sup> The optical emission energies of Sn-related defects in  $\beta\text{-Ga}_2\text{O}_3$  were estimated using hybrid functional calculations. The epitaxial growth, fabrication, and characterization experimental details are described in the [supplementary material](#), Annexure-A.

To evaluate relative defect solubilities and associated defect level positions, defect formation energies ( $E^f$ ) and thermodynamic and vertical transition levels were calculated using the Heyd-Scuseria-Ernzshof screened hybrid functional (HSE06) and the projector-augmented wave (PAW) approach as implemented in the VASP code.<sup>16–19</sup> All calculations were performed using supercells with 160-atoms with the same computational approach and finite size corrections for the formation energies and thermal and vertical transition energies as detailed in other previous publications.<sup>20–22</sup> Configuration coordinate diagrams were constructed with the calculated energies and used to evaluate the resulting optical excitation and emission energies to compare with the experimental spectra. To assess uncertainties in the reduction of the bandgap with Sn-alloying, we provide additional estimates of calculated emission energies, assuming the observed redshift in the bandgap occurs in the conduction band only vs including contributions to changes in the valence band position. These choices lead to additional uncertainties in the calculated energies by approximately 0.1 eV.

Figure 1(a) shows a cross section schematic of epilayers and real images of fabricated devices/sample, while the [supplementary material](#), Fig. S1, shows the surface morphology. The XRD plot in Fig. 1(b) shows that the TGO epilayers are monoclinic in nature, following the  $\text{Ga}_2\text{O}_3$  substrate with the major peaks aligned. The two extra peaks at  $\sim 30.28^\circ$  and  $\sim 44.37^\circ$  of the TGO film might be the  $(-402)$  and  $(-604)$  planes of monoclinic TGO epilayer, respectively. However, with the limited XRD database of TGO, it is hard to attribute the right orientation. Thus, we performed cross-sectional HRTEM where we observed that the orientation is slightly modified from monoclinic phase, which needs to be studied further, not the scope of this paper. The tin concentration variation was not much among the samples, and, consequently, we have not observed any peak shifting in XRD as we saw in TGO on  $(010)$   $\beta\text{-Ga}_2\text{O}_3$ ,<sup>5</sup> sapphire,<sup>4</sup> and silicon<sup>6</sup> substrates. The Tauc plot in Fig. S2 shows the estimation of the bandgap for various Sn concentrations. This bandgap along with Sn% found by WDX plotted in Fig. 1(c) with the MBE Ga/Sn flux-ratio. A redshift in the bandgap is observed as the Sn incorporation in the TGO is increased. Compositionally, uniform epilayer is evident in Fig. S3 WDX cross-sectional images.

The high-angle annular dark-field (HAADF) from HRTEM images in Figs. 2(a) and 2(b) clearly show the thickness of the epilayer as 500 nm as well as the film quality. Figures 2(c) and 2(d) present the selected area diffraction pattern (SADP) for the substrate and TGO epilayer, respectively. When the two SADP images are compared, the growth plane in the film is the same, but additional spots appear in the

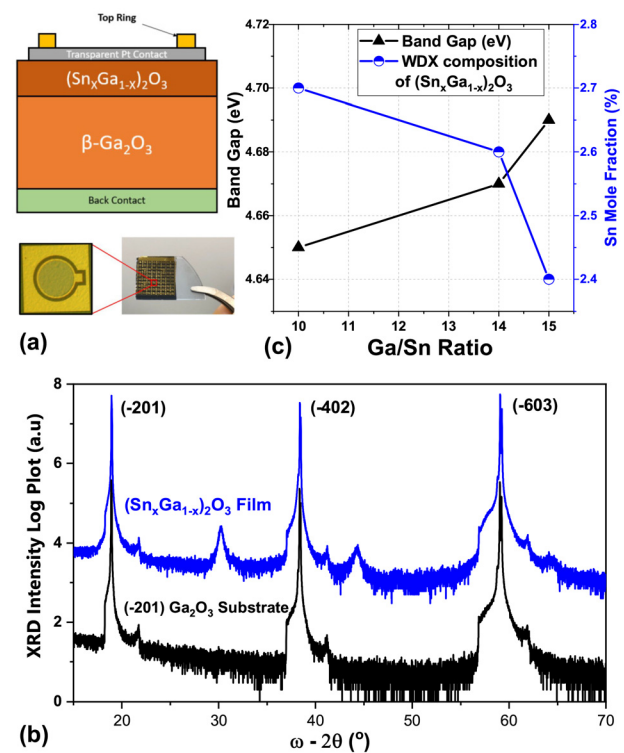


FIG. 1. (a) Schematic of epilayers and fabricated real image of device/sample, (b) comparative XRD, and (c) bandgap and Sn% with MBE flux-ratio.

middle of two adjacent  $(-201)_{\text{sub}}$  diffraction spots. Both diffraction patterns are parallel to  $(010)_{\text{sub}}$ , which is in the growth plane. The  $(201)_{\text{sub}}$  plane is nearly perpendicular to the growth direction, which is used to speculate the in-plane orientation relationship between the film and substrate. Figure 2(e) is the schematic of SADP in the  $[010]$

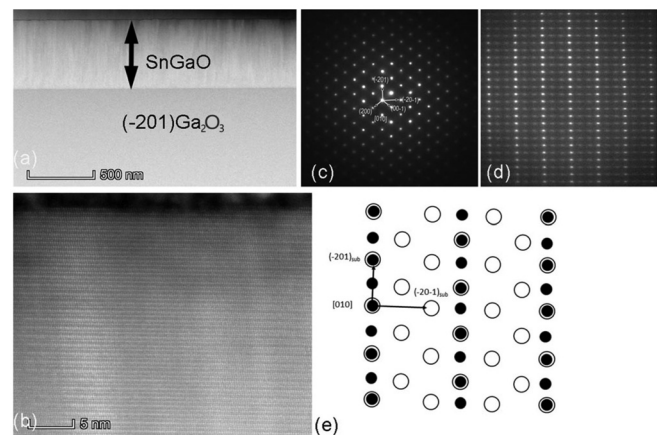


FIG. 2.  $[010]$  Cross-sectional TEM images of the TGO film and the substrate. (a) and (b) HAADF images with different magnifications. (c) and (d) SADPs taken from substrate and film, respectively. (e) Schematic of SADP; the white spots correspond to the diffraction pattern from substrate, and the black spots refer to strong diffraction from the TGO film.

direction for both film and substrate. The black spots refer to strong diffraction from film, while white spots refer to diffraction from substrate. The diffraction spots, mainly perpendicular to the growth direction for the film, not only are parallel to  $(201)_{\text{sub}}$  but also show a 2:3 spacing ratio. All of the observation and analysis indicate that the microstructure of the film has changed due to Sn-alloying. This is likely due to the interplay between the concentrations of incorporated donors like Sn, compensating  $V_{\text{Ga}}$  species, and their connection to structural defects or alternative phases inclusions like the  $\gamma$ -phase.<sup>23,24</sup> While, in this work, we focus on the Sn-related defects in the  $\beta$ -phase as an initial proxy to understand the origins of the observed emission-bands and measured optical response, further work is needed to better resolve the structure and clarify its role in the device performance and optical behavior.

Figure 3(a) shows the I-V characteristics for a 500  $\mu\text{m}$  diameter device of the highest responsivity sample (35 kA/W) in the dark and under UV illumination. Figure S4 provides the measured spectral response of different devices at  $-5\text{ V}$ . We observe a clear redshift in the 1-dB cutoff below 280 nm as the Sn% increases, consistent with our prior works.<sup>4–6</sup> The absolute spectral responsivity of the optimized sample in Fig. 3(b) validates the solar-blind functionality. Transient measurements, shown in Fig. 3(c), were fitted with a double exponential to determine the  $\tau_1$  and  $\tau_2$  times for both the rise and fall segments. The devices'  $\tau_1$  fall times were considerably shorter, with all devices having values in the milliseconds regime. Achieving millisecond order rise/fall times at an extremely high responsivity of 35 kA/W makes TGO devices very fast compared to its counterparts because of the tradeoff<sup>14</sup> between response time and gain in the system in the  $\text{Ga}_2\text{O}_3$ -based Schottky barrier photodetectors.

The optimized sample shows an ultra-high peak responsivity of  $3.5 \times 10^4\text{ A/W}$ , implying that there is a clear gain mechanism since External Quantum Efficiency (EQE) cannot be more than unity. These high-gains are attributed to three main mechanisms in the literature: Impact ionization, Self-Trapped holes (STHs), and hole-trapping in the space-charge region (SCR) in Schottky-barrier diodes. Impact

ionization requires a high electric field in the SCR; however, it is not the case with low bias voltages (only  $-5\text{ V}$  in this work). Likewise, STHs are thermally unstable above 90 K,<sup>25</sup> and a 0.40 eV barrier was calculated for migration of STHs.<sup>26</sup> Therefore, they may not have a noticeable effect at RT. Hole-trapping at the SCR is considered to be the root of the high photoconductive gain by means of deep-level defect states, especially  $V_{\text{Ga}}$ .<sup>6,8</sup> Therefore, we propose that Sn-alloying introduces deep-level defects rather than irradiation with fast reactor neutrons, 20 MeV protons, or treatment in high ion density Ar-plasma.<sup>9</sup> This is also consistent with prior reports that confirm the expected correlation between incorporated donor concentrations and native sources of compensation like  $V_{\text{Ga}}$  deep acceptors that can readily trap holes.<sup>21,23,24,27,28</sup> To further investigate the deep-level defects, we performed CL spectroscopy and HSI.

Peak positions of all the TGO samples appeared same as shown in Fig. 4(a). It also clearly shows the appearance of peaks (mid-gap donor/acceptor level) at blue ( $\sim 2.50$ – $2.75\text{ eV}$ ) and green bands ( $\sim 2.10$ – $2.25\text{ eV}$ ), which are not present in the substrate. Deconvolving the spectra identifies the peak positions as  $\sim 2.64$  and  $\sim 2.20\text{ eV}$ , which can clearly be seen in Fig. 4(b) where the normalized CL intensities are plotted for both the TGO films and the substrate.

Moreover, in the TGO films, the UV-range peak intensity is lower and that of the blue emission is greater compared to the  $\text{Ga}_2\text{O}_3$  substrate. We have not observed any definite correlation between CL peak intensity variations with Sn% among the samples. Intrinsic point-defects in  $\text{Ga}_2\text{O}_3$  such as  $V_{\text{Ga}}$  and oxygen vacancies ( $V_{\text{O}}$ ) exhibit distinct dependencies on the ambient, doping, and defect concentrations, and their relative populations can influence the absorption and luminescence characteristics.<sup>29–33</sup> In Fig. 4(b), the UV band is found to be diminished in the TGO film relative to the bulk  $\text{Ga}_2\text{O}_3$ , which indicates the enhancement of other recombination channels not associated with intrinsic hole-trapping in the form of STHs.<sup>32</sup> Regarding the second intrinsic point defect, we first note that the TGO films are found to be modestly n-type by Capacitance-Voltage (CV) measurement ( $n \sim 10^{17}\text{ cm}^{-3}$ ), despite their large Sn concentration. This suggests significant compensation of incorporated Sn donors, consistent with the formation of a larger number of compensating acceptor species such as  $V_{\text{Ga}}$  that become more favorable in n-type conditions.<sup>21,23,24,27,28,34</sup>  $V_{\text{Ga}}$  is also known to form a number of complexes with other intrinsic and extrinsic donor defects such as  $V_{\text{O}}$ , H, <sup>35,36</sup> and Sn<sup>23,28</sup> because of the Coulomb attraction between positively charged donors and the triply negatively charged  $V_{\text{Ga}}$ . This results in highly stable complexes with large binding energies such as 1.63 eV for the most stable forms of  $V_{\text{Ga}}$ -Sn complexes in n-type material. We have mentioned earlier that the 2.20 and 2.64 eV peaks are not present in neither the  $\text{Ga}_2\text{O}_3$  substrate nor the MBE grown  $\text{Ga}_2\text{O}_3$  homoepitaxial layer. The incorporation of Sn donors into the  $\text{Ga}_2\text{O}_3$  crystal lattice may well have increased the concentration of compensatory  $V_{\text{Ga}}$  and  $V_{\text{Ga}}$ -Sn complexes, which will be investigated in the subsequent paragraphs.

To further interrogate the role of Sn, WDX and CL HSI were performed as shown in Fig. 5. The observed emission spectra are uniform over the cross section of the TGO epilayers. Figure 5(a) shows a map of the Sn WDX counts identifying the TGO layer and the  $\text{Ga}_2\text{O}_3$  substrate. The UV-blue emission peak intensity is reduced in the presence of Sn as shown in Figs. 5(b) and 5(c). In addition, Fig. 5(d) demonstrates that the green emission peak is consolidated in the TGO film, with an intensity far greater than in the Sn-doped substrate, which is

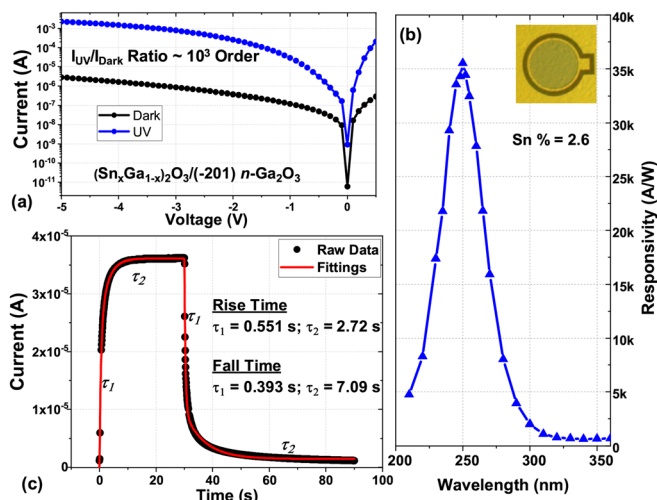


FIG. 3. (a) I-V characteristics, (b) spectral responsivity of the highest responsivity sample, and (c) transient with curve fittings.



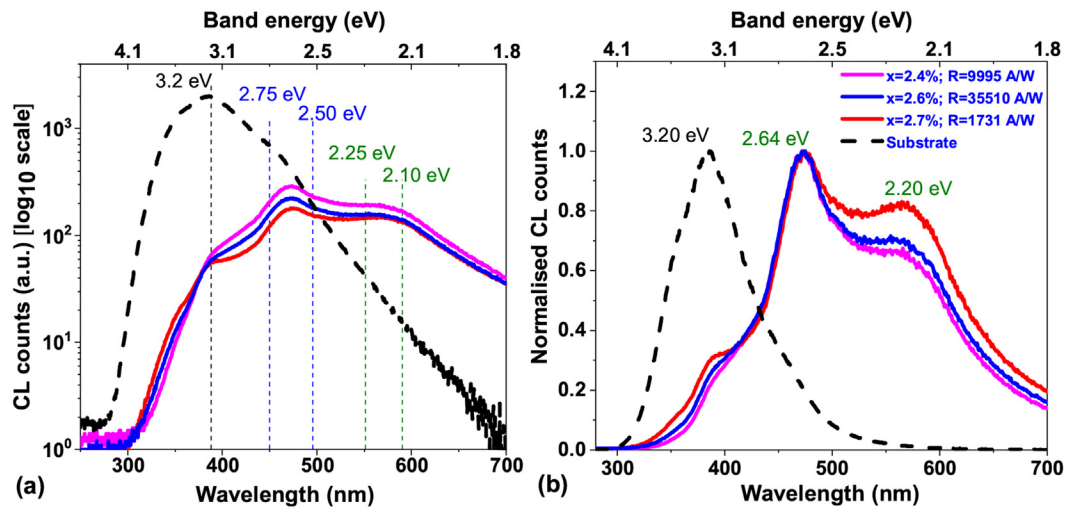


FIG. 4. Comparative CL spectra from TGO samples and Ga<sub>2</sub>O<sub>3</sub> substrate excited using a 6 keV electron beam: (a) absolute CL intensity in log<sub>10</sub> scale and (b) normalized intensity.

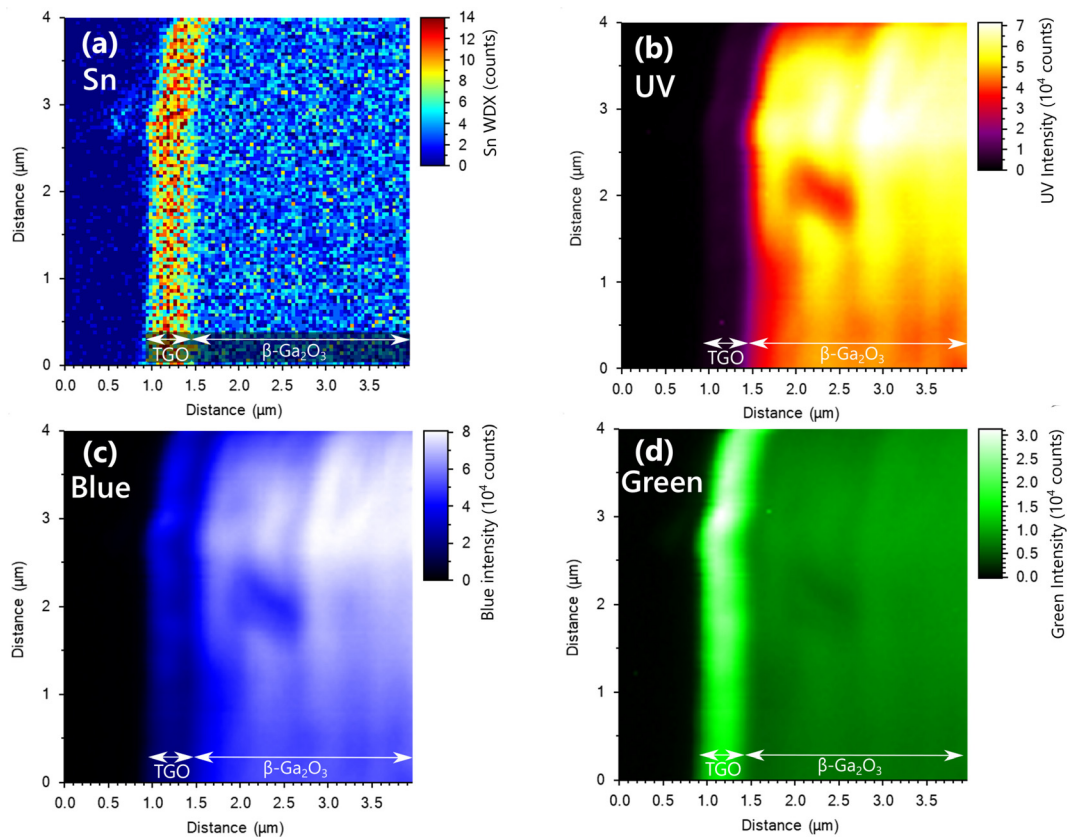


FIG. 5. Cross-sectional WDX and CL-HSI of the TGO film ( $x = 2.6\%$ ) and the substrate. Images showing the intensity of (a) Sn WDX x-ray counts, and emission peaks of (b) UV, (c) blue, and (d) green.

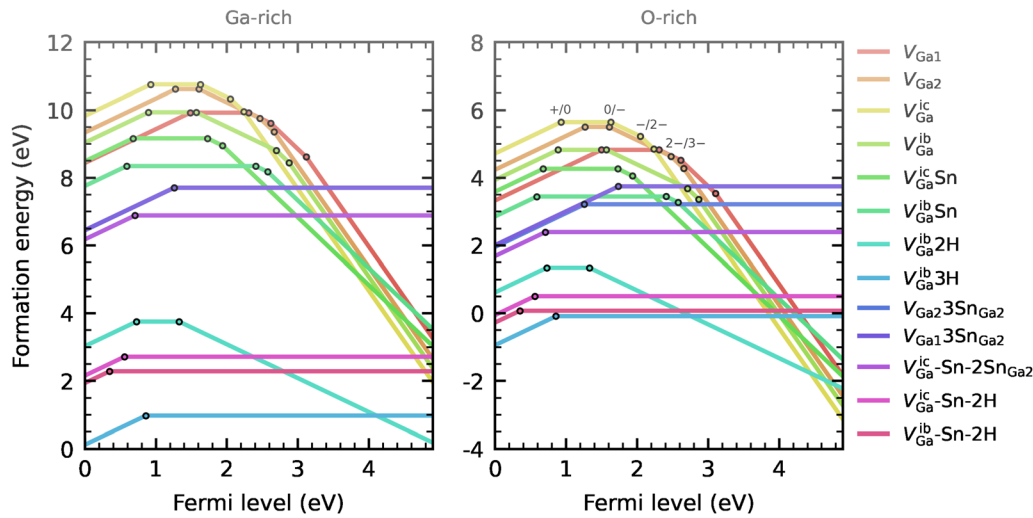


FIG. 6. Formation energy diagram for  $V_{Ga}$  and related complexes with H and Sn shown for (a) Ga-rich and (b) O-rich conditions.

further evidence of this emission peak being related to Sn and/or  $V_{Ga}$  complexes, as previously stated.

Figure 6 plots the calculated formation energies for  $V_{Ga}$  and a number of complexes that may form with H and/or Sn. We primarily consider the displaced or “split” vacancy configurations (e.g.,  $V_{Ga}^{ic}$  and  $V_{Ga}^{ib}$ ) that have been previously shown to be favorable configurations for isolated  $V_{Ga}$  and their complexes with H and Sn.<sup>23,27,35</sup> These complexes can form with Sn or Ga as the displaced atom that occupies the interstitial position (ic or ib) with  $Sn^{ic}$  or  $Sn^{ib}$  being the more thermodynamically preferable configurations and labeled in Fig. 6 as  $V_{Ga}^{ic-Sn}$  or  $V_{Ga}^{ib-Sn}$ , respectively. We also include formation energies for  $V_{Ga}$  on the tetrahedral ( $Ga_T$ ) and octahedral ( $Ga_{II}$ ) sites, with different neighboring Sn  $Ga_{II}$  configurations. These results illustrate the strong driving force to form compensating  $V_{Ga}$  acceptor complexes as the Fermi level is pushed to more n-type conditions, and how fully passivated complexes can also be favorable (e.g.,  $V_{Ga}-3H$ ,  $V_{Ga}-3Sn_{Ga}$ , and  $V_{Ga}-Sn_{Ga}-2H$ , among others). Table I presents the calculated emission for the defects, from which we find the best matches for the 2.64 eV band in the TGO films that result from electron recombination with trapped hole states associated with a number of different vacancy configurations. In particular, we find that recombination of a free electron with a hole trapped on isolated  $(V_{Ga}^{ic})^+$  and  $(V_{Ga}^{ib})^+$  configurations or their complexes with Sn [e.g.,  $(V_{Ga}^{ic}-Sn)^+$ ] exhibit an emission between  $\sim 2.6$  and 2.7 eV. This is consistent with previous theoretical calculations reporting emission  $\sim 2.6$  eV for  $V_{Ga}-Sn$  complexes.<sup>28</sup> However, we find the donor charge-states of these defects to be unlikely in n-type conditions, as they would need to be ionized from the  $-3$  charge-state, and, thus, consider other more passivated forms such as the  $V_{Ga}$  decorated with one or more Sn. Indeed, we find that analogs such as a  $V_{Ga}-Sn^{ic}$  complex with 1 or 2 neighboring  $Sn_{Ga}$  form more passivated centers in n-type conditions that exhibit  $\sim 2.6$  eV emission-bands for free electrons recombining with holes trapped at these centers. This suggests that under optical excitation, hole-trapping at a number of different defects such as these  $V_{Ga}$  complexes that are enhanced in the TGO can lead to the 2.6 eV emission-band.

For the 2.20 eV band, we find a qualitatively analogous origin as the 2.64 eV band but originating from defects involving  $V_{Ga_{II}}$

orientations rather than the split-vacancy configurations. For example, we find the best agreement from the studied defects to be from the recombination of free electrons with holes trapped at the  $V_{Ga_{II}}^+$  donor-state or the fully passivated  $V_{Ga_{II}}-3Sn_{Ga}$  complex yielding emission

TABLE I. CC model parameters for  $V_{Ga}$  complexed with Sn and H donors, including zero phonon line (ZPL) energy ( $E_{ZPL}$ ), classical emission ( $E_{em}$ ), and absorption ( $E_{abs}$ ) energies and total mass-weighted distortion ( $\Delta Q$ ). Obtained from HSE(0.33,0.20) dv calculations.

Optical transition	$E_{ZPL}$ (eV)	$E_{em}$ (eV)	$E_{abs}$ (eV)	$\Delta Q$ (amu <sup>1/2</sup> /Å)
$(V_{Ga}^{ib})^+ + e_{CBM}^-$	4.25	2.69	5.1	2.67
$(V_{Ga}^{ic})^+ + e_{CBM}^-$	3.97	2.56	5	2.81
$V_{Ga2}^+ + e_{CBM}^-$	3.62	2.16	4.92	2.79
$V_{Ga1}^+ + e_{CBM}^-$	3.4	1.94	4.75	2.47
$(V_{Ga}^{ic}-Sn)^+ + e_{CBM}^-$	2.95	1.51	4.27	2.42
$(V_{Ga}^{ic}-Sn)^0 + e_{CBM}^-$	3.17	1.62	4.48	2.46
$(V_{Ga}^{ic}-Sn)^- + e_{CBM}^-$	4.16	2.7	5.16	2.78
$(V_{Ga}^{ib}-Sn)^- + e_{CBM}^-$	2.32	0.91	3.67	2.34
$(V_{Ga}^{ib}-Sn)^0 + e_{CBM}^-$	2.49	1.1	3.83	2.35
$(V_{Ga}^{ib}-Sn)^+ + e_{CBM}^-$	4.31	2.73	5.05	2.74
$(V_{Ga}^{ic}-Sn-Sn_{Ga2})^0 + e_{CBM}^-$	3.22	1.83	4.45	2.41
$(V_{Ga}^{ic}-Sn-Sn_{Ga2})^+ + e_{CBM}^-$	4.07	2.64	5.09	2.82
$(V_{Ga}^{ic}-Sn-2Sn_{Ga2})^+ + e_{CBM}^-$	4	2.61	5.11	2.86
$(V_{Ga2}2Sn_{Ga2})^0 + e_{CBM}^-$	3.14	1.8	4.33	2.03
$(V_{Ga2}3Sn_{Ga2})^+ + e_{CBM}^-$	3.64	2.23	4.83	2.15
$(V_{Ga1}3Sn_{Ga2})^+ + e_{CBM}^-$	3.15	1.79	4.36	2.19
$(V_{Ga}^{ib}2H)^0 + e_{CBM}^-$	3.57	2	4.81	2.59
$(V_{Ga}^{ib}3H)^+ + e_{CBM}^-$	3.95	2.5	5.1	2.7
$(V_{Ga}^{ib}-Sn-H)^0 + e_{CBM}^-$	2.52	1.12	2.83	2.28
$(V_{Ga}^{ic}-Sn-H)^0 + e_{CBM}^-$	3.2	1.77	4.49	2.47
$(V_{Ga}^{ib}-Sn-2H)^+ + e_{CBM}^-$	4.54	2.97	5.07	2.82
$(V_{Ga}^{ic}-Sn-2H)^+ + e_{CBM}^-$	4.33	2.86	5.04	2.7

energies of 2.16 and 2.23 eV, respectively. We note that the binding-energies of  $V_{\text{GaII}}$  with multiple Sn are reasonably large, with the third Sn-binding more stable by 0.94 eV relative to isolated ( $V_{\text{GaII}}-2\text{Sn}_{\text{Ga}}^-$  and  $\text{Sn}_{\text{Ga}}^+$ ), suggesting these complexes are likely to be stable if formed. Considering this modest complex binding strength, the high surface mobility of Sn,<sup>37</sup> and the large degree of compensation of the incorporated Sn in the TGO films, these complexes are likely candidates for the 2.20 eV band. This may also be supported by the lower relative intensities of the 2.20 eV band, as the split-vacancy configurations are predicted to be more thermodynamically favorable and likely to form in higher concentrations in the absence of other kinetic hindrances that may result from complexing. Finally, we note that the presence of interstitial H and its passivation of  $V_{\text{Ga}}$  and  $V_{\text{Ga}}-\text{Sn}$  complexes may also influence the relative stability of these defects and their charge-states and may contribute to shifts in some of the emission-bands as seen in Table I. While Sn-related defects are expected to dominate in these samples based on their concentrations, the effects of H on these bands will be investigated in more detail in future publications.

Among the three gain mechanisms mentioned, impact ionization and STHs are not likely contributors. Hole-trapping at the deep-level defects in the SCR is considered to be the root of the high photoconductive gain by lowering the Schottky barrier height in  $\text{Ga}_2\text{O}_3$ .<sup>8</sup> Recently, we reported TGO on Si films showing enhanced blue and green emissions, which was attributed to the deep-level acceptors.<sup>6</sup> This correlation and the gain are higher in the present work along with faster PDs, thanks to the single crystal TGO epilayer. Moreover, based on hybrid functional calculations of the optical emission expected for defects involving Sn in  $\beta\text{-Ga}_2\text{O}_3$ ,  $V_{\text{Ga}}-\text{Sn}$  complexes with the possibility of additional  $\text{H}_i$  are proposed as potential defect origins of the observed green and blue emission-bands. These complexes increase the deep-level trap states and can serve as hole-trapping centers as illustrated in Fig. 7. The accumulated holes in the SCR via trapping to the deep acceptor sites increase the total positive charge. Thereby, the electric field in the SCR increases. Higher surface electric field ( $E_{\text{max}}$ ) lowers the Schottky barrier via image-force lowering [ $\Delta\Phi_b = \sqrt{(qE_{\text{max}}/4\pi\epsilon_s)}$ ] and thins the barrier width.<sup>38</sup> Thereby, it exponentially enhances thermionic emission and the probability of

electron tunneling, which leads to high gains as demonstrated in this work. Li *et al.* have demonstrated that near-ideal barrier tunneling governs dark current characteristics for  $E_{\text{max}}$  greater than 0.8 MV/cm.<sup>39</sup> They also investigated the electric-field threshold (ET) above which the dominant current mechanism switches from thermionic emission to electron tunneling.<sup>40</sup> They found that at RT, ET is about 0.3 MV/cm, which means that even at moderate electric fields, electron tunneling is an effective mechanism. Given adequate hole-trapping at the aforementioned deep-level acceptors, both the Schottky effect and electron tunneling may be the major sources in the gain mechanism of TGO Schottky-barrier photodetectors. Furthermore, alloying broadens the UV-C coverage and increases the bandwidth of the resultant photodetector.

In conclusion, the TGO planar solar-blind Schottky photodetector demonstrated a record-setting responsivity of 35 510 A/W at  $-5$  V. Defect-induced mid-bandgap donor/acceptor levels were found to be playing a key role in trapping holes and thereby enhancing the photoconductive gain. RTCL spectra and HSI depict clear peak appearances at 2.64 and 2.20 eV, respectively, which are not present in the  $\text{Ga}_2\text{O}_3$  substrate as well as the MBE-grown  $\text{Ga}_2\text{O}_3$  homoepitaxial layer. UV-emission-bands in the substrate and  $\text{Ga}_2\text{O}_3$  epilayers are suppressed in the TGO films, suggesting either a redistribution of defect populations and/or preferential recombination channels. The first principles calculations identify the nature of defect levels to be  $V_{\text{Ga}}$  complexes with one or more Sn and possibly H that lead to passivated complexes that can trap holes and lead to the dominant emission-bands in the TGO films. Hole-trapping at these deep-level defects in the SCR is found to be responsible for the exponential increase in photocurrent by lowering the Schottky barrier height via the Schottky effect, and electron tunneling via lowering the barrier height and thinning the barrier width. This study investigates how Sn influences the mid-bandgap defect levels and enhances the figure-of-merit of the photodetector, which is much superior to its planar device counterparts and possesses record-high responsivity for the UV-C solar-blind photodetector.

See the [supplementary material](#) for the details of the growth, fabrication, and characterization experiments. Furthermore, we presented results and analysis from various experiments like secondary electron imaging (Fig. S1), room temperature optical bandgap estimations (Fig. S2), WDX mapping (Fig. S3), and spectral responsivity measurements (Fig. S4). In addition, further device parameters (Table S1) and intensity-dependent responsivity (Fig. S5) and response time (Fig. S6) are included to depict opto-electronic proprieties of the photodetectors.

W.V.S., P.M., and I.H. would like to acknowledge support from the Army Research Office, monitored by Dr. Michael Gerhold. I.H. was supported by the Ministry of National Education of the Republic of Türkiye. This work was partly supported by the EPSRC project “Nanoanalysis for Advanced Materials and Healthcare” (No. EP/N010914/1). The work by J.B.V. was partially performed under the auspices of the U.S. DOE by Lawrence Livermore National Laboratory under Contract No. DE-AC52-07NA27344 and partially supported by the Critical Materials Institute and LLNL LDRD funding under Project No. 22-SI-003. Y.K.F. was supported by the Research Council of Norway through the GO-POW project (Grant No. 314017).

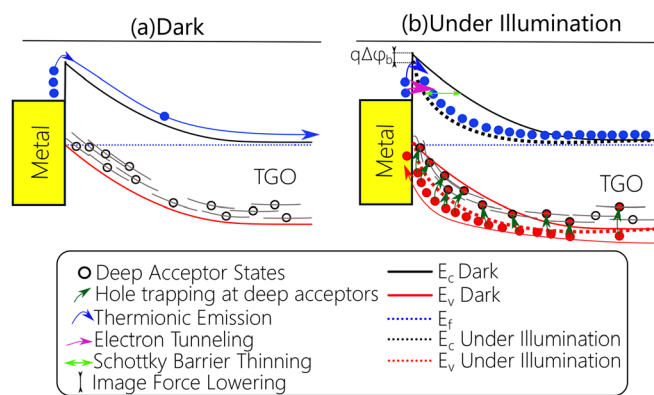


**FIG. 7.** The proposed gain mechanism via deep-level acceptor states introduced by Sn incorporation into the  $\text{Ga}_2\text{O}_3$  crystal lattice. (a) Carrier transport in TGO under dark conditions. (b) Hole-trapping-assisted gain mechanism under UV illumination in TGO photodetectors.



## AUTHOR DECLARATIONS

## Conflict of Interest

The authors have no conflicts to disclose.

## Author Contributions

**Partha Mukhopadhyay:** Conceptualization (lead); Data curation (equal); Formal analysis (equal); Investigation (equal); Methodology (equal); Supervision (equal); Writing – original draft (equal); Writing – review & editing (equal). **Feng Wu:** Data curation (equal); Formal analysis (equal); Methodology (equal); Writing – original draft (equal). **Akhil Mauze:** Data curation (equal); Formal analysis (equal); Writing – original draft (equal). **James S. Speck:** Formal analysis (equal); Investigation (equal); Methodology (equal); Supervision (equal); Writing – original draft (equal); Writing – review & editing (equal). **Winston V. Schoenfeld:** Conceptualization (equal); Formal analysis (equal); Funding acquisition (equal); Investigation (equal); Methodology (equal); Project administration (equal); Supervision (equal); Writing – original draft (equal); Writing – review & editing (equal). **Isa Hatipoglu:** Conceptualization (equal); Data curation (equal); Formal analysis (equal); Investigation (equal); Methodology (equal); Writing – original draft (equal); Writing – review & editing (equal). **Ymir Kalmann Frodason:** Data curation (equal); Formal analysis (equal); Methodology (equal); Software (equal); Writing – original draft (equal); Writing – review & editing (equal). **Joel Basile Varley:** Data curation (equal); Formal analysis (equal); Investigation (equal); Methodology (equal); Software (equal); Supervision (equal); Writing – original draft (equal); Writing – review & editing (equal). **Martin S. Williams:** Data curation (equal); Formal analysis (equal); Methodology (equal); Writing – original draft (equal). **Daniel A. Hunter:** Data curation (equal); Formal analysis (equal); Methodology (equal); Writing – original draft (equal); Writing – review & editing (equal). **Naresh Kumar Gunasekar:** Data curation (equal); Formal analysis (equal); Investigation (equal); Methodology (equal); Writing – original draft (equal); Writing – review & editing (equal). **Paul R. Edwards:** Data curation (equal); Formal analysis (equal); Methodology (equal); Writing – original draft (equal); Writing – review & editing (equal). **Robert W. Martin:** Formal analysis (equal); Investigation (equal); Methodology (equal); Writing – original draft (equal); Writing – review & editing (equal).

## DATA AVAILABILITY

The data that support the findings of this study are available within the article and its [supplementary material](#).

## REFERENCES

- T. Onuma, S. Saito, K. Sasaki, T. Masui, T. Yamaguchi, T. Honda, and M. Higashiwaki, "Valence band ordering in  $\beta$ -Ga<sub>2</sub>O<sub>3</sub> studied by polarized transmittance and reflectance spectroscopy," *Jpn. J. Appl. Phys., Part 1* **54**, 112601 (2015).
- I. Hatipoglu, P. Mukhopadhyay, F. Alema, T. S. Sakthivel, S. Seal, A. Osinsky, and W. V. Schoenfeld, "Tuning the responsivity of monoclinic solar-blind photodetectors grown by metal organic chemical vapor deposition," *J. Phys. D* **53**, 454001 (2020).
- T. Oshima, T. Okuno, N. Arai, Y. Kobayashi, and S. Fujita, " $\beta$ -Al<sub>2</sub>Ga<sub>2-2x</sub>O<sub>3</sub> thin film growth by molecular beam epitaxy," *Jpn. J. Appl. Phys., Part 1* **48**, 070202 (2009).
- P. Mukhopadhyay and W. V. Schoenfeld, "Tin gallium oxide solar-blind photodetectors on sapphire grown by molecular beam epitaxy," *Appl. Opt.* **58**, D22–D27 (2019).
- P. Mukhopadhyay and W. V. Schoenfeld, "High responsivity tin gallium oxide Schottky ultraviolet photodetectors," *J. Vac. Sci. Technol., A* **38**, 013403 (2020).
- I. Hatipoglu, D. A. Hunter, P. Mukhopadhyay, M. S. Williams, P. R. Edwards, R. W. Martin, W. V. Schoenfeld, and G. Naresh-Kumar, "Correlation between deep-level defects and functional properties of  $\beta$ -(Sn<sub>x</sub>Ga<sub>1-x</sub>)<sub>2</sub>O<sub>3</sub> on Si photodetectors," *J. Appl. Phys.* **130**, 204501 (2021).
- P. Mukhopadhyay, I. Hatipoglu, T. S. Sakthivel, D. A. Hunter, P. R. Edwards, R. W. Martin, G. Naresh-Kumar, S. Seal, and W. V. Schoenfeld, "High figure-of-merit gallium oxide UV photodetector on silicon by molecular beam epitaxy: A path toward monolithic integration," *Adv. Photonics Res.* **2**, 2000067 (2021).
- E. Yakimov, A. Polyakov, I. Shchemerov, N. Smirnov, A. Vasilev, P. Vergeles, E. Yakimov, A. Chernykh, A. Shikoh, F. Ren *et al.*, "Photosensitivity of Ga<sub>2</sub>O<sub>3</sub> Schottky diodes: Effects of deep acceptor traps present before and after neutron irradiation," *APL Mater.* **8**, 111105 (2020).
- E. Yakimov, A. Polyakov, I. Shchemerov, N. Smirnov, A. Vasilev, A. Kochkova, P. Vergeles, E. Yakimov, A. Chernykh, M. Xian *et al.*, "On the nature of photosensitivity gain in Ga<sub>2</sub>O<sub>3</sub> Schottky diode detectors: Effects of hole trapping by deep acceptors," *J. Alloys Compd.* **879**, 160394 (2021).
- D. Gunkel, D. V. Christensen, Y. Chen, and N. Pryds, "Oxygen vacancies: The (in)visible friend of oxide electronics," *Appl. Phys. Lett.* **116**, 120505 (2020).
- H. J. Queisser and E. E. Haller, "Defects in semiconductors: Some fatal, some vital," *Science* **281**, 945–950 (1998).
- P. R. Edwards and R. W. Martin, "Cathodoluminescence nano-characterization of semiconductors," *Semicond. Sci. Technol.* **26**, 064005 (2011).
- H. Y. Hwang, Y. Iwasa, M. Kawasaki, B. Keimer, N. Nagaosa, and Y. Tokura, "Emergent phenomena at oxide interfaces," *Nat. Mater.* **11**, 103–113 (2012).
- D. Kaur and M. Kumar, "A strategic review on gallium oxide based deep-ultraviolet photodetectors: Recent progress and future prospects," *Adv. Opt. Mater.* **9**, 2002160 (2021).
- P. R. Edwards, L. K. Jagadamma, J. Bruckbauer, C. Liu, P. Shields, D. Allsopp, T. Wang, and R. W. Martin, "High-resolution cathodoluminescence hyperspectral imaging of nitride nanostructures," *Microsc. Microanal.* **18**, 1212–1219 (2012).
- J. Heyd, G. E. Scuseria, and M. Ernzerhof, "Hybrid functionals based on a screened coulomb potential," *J. Chem. Phys.* **118**, 8207–8215 (2003).
- P. E. Blöchl, "Projector augmented-wave method," *Phys. Rev. B* **50**, 17953 (1994).
- G. Kresse and J. Furthmüller, "Efficiency of ab-initio total energy calculations for metals and semiconductors using a plane-wave basis set," *Comput. Mater. Sci.* **6**, 15–50 (1996).
- G. Kresse and J. Furthmüller, "Efficient iterative schemes for *ab initio* total-energy calculations using a plane-wave basis set," *Phys. Rev. B* **54**, 11169 (1996).
- C. Freysoldt, B. Grabowski, T. Hickel, J. Neugebauer, G. Kresse, A. Janotti, and C. G. Van de Walle, "First-principles calculations for point defects in solids," *Rev. Mod. Phys.* **86**, 253 (2014).
- Y. K. Frodason, K. Johansen, L. Vines, and J. Varley, "Self-trapped hole and impurity-related broad luminescence in  $\beta$ -Ga<sub>2</sub>O<sub>3</sub>," *J. Appl. Phys.* **127**, 075701 (2020).
- T. Gake, Y. Kumagai, C. Freysoldt, and F. Oba, "Finite-size corrections for defect-involving vertical transitions in supercell calculations," *Phys. Rev. B* **101**, 020102 (2020).
- J. M. Johnson, Z. Chen, J. B. Varley, C. M. Jackson, E. Farzana, Z. Zhang, A. R. Arehart, H.-L. Huang, A. Genc, S. A. Ringel *et al.*, "Unusual formation of point-defect complexes in the ultrawide-band-gap semiconductor  $\beta$ -Ga<sub>2</sub>O<sub>3</sub>," *Phys. Rev. X* **9**, 041027 (2019).
- C. S. Chang, N. Tanen, V. Protasenko, T. J. Asel, S. Mou, H. G. Xing, D. Jena, and D. A. Muller, " $\gamma$ -phase inclusions as common structural defects in alloyed  $\beta$ -(Al<sub>x</sub>Ga<sub>1-x</sub>)<sub>2</sub>O<sub>3</sub> and doped  $\beta$ -Ga<sub>2</sub>O<sub>3</sub> films," *APL Mater.* **9**, 051119 (2021).
- B. E. Kananen, N. C. Giles, L. E. Halliburton, G. Foundos, K. Chang, and K. Stevens, "Self-trapped holes in  $\beta$ -Ga<sub>2</sub>O<sub>3</sub> crystals," *J. Appl. Phys.* **122**, 215703 (2017).



- <sup>26</sup>J. B. Varley, A. Janotti, C. Franchini, and C. G. Van de Walle, "Role of self-trapping in luminescence and p-type conductivity of wide-band-gap oxides," *Phys. Rev. B* **85**, 081109 (2012).
- <sup>27</sup>M. E. Ingebrigtsen, A. Y. Kuznetsov, B. G. Svensson, G. Alfieri, A. Mihaila, U. Badstübner, A. Perron, L. Vines, and J. B. Varley, "Impact of proton irradiation on conductivity and deep level defects in  $\beta$ -Ga<sub>2</sub>O<sub>3</sub>," *APL Mater.* **7**, 022510 (2019).
- <sup>28</sup>A. Singh, O. Koksai, N. Tanen, J. McCandless, D. Jena, H. G. Xing, H. Peelaers, and F. Rana, "Ultrafast dynamics of gallium vacancy charge states in  $\beta$ -Ga<sub>2</sub>O<sub>3</sub>," *Phys. Rev. Res.* **3**, 023154 (2021).
- <sup>29</sup>M. D. McCluskey, "Point defects in Ga<sub>2</sub>O<sub>3</sub>," *J. Appl. Phys.* **127**, 101101 (2020).
- <sup>30</sup>H. Peelaers, J. L. Lyons, J. B. Varley, and C. G. Van de Walle, "Deep acceptors and their diffusion in Ga<sub>2</sub>O<sub>3</sub>," *APL Mater.* **7**, 022519 (2019).
- <sup>31</sup>Z. Wang, X. Chen, F.-F. Ren, S. Gu, and J. Ye, "Deep-level defects in gallium oxide," *J. Phys. D* **54**, 043002 (2021).
- <sup>32</sup>Q. D. Ho, T. Frauenheim, and P. Deák, "Origin of photoluminescence in  $\beta$ -Ga<sub>2</sub>O<sub>3</sub>," *Phys. Rev. B* **97**, 115163 (2018).
- <sup>33</sup>C. Zimmermann, V. Rønning, Y. K. Frodason, V. Bobal, L. Vines, and J. Varley, "Primary intrinsic defects and their charge transition levels in  $\beta$ -Ga<sub>2</sub>O<sub>3</sub>," *Phys. Rev. Mater.* **4**, 074605 (2020).
- <sup>34</sup>T. Zacherle, P. Schmidt, and M. Martin, "Ab initio calculations on the defect structure of  $\beta$ -Ga<sub>2</sub>O<sub>3</sub>," *Phys. Rev. B* **87**, 235206 (2013).
- <sup>35</sup>J. B. Varley, H. Peelaers, A. Janotti, and C. G. Van de Walle, "Hydrogenated cation vacancies in semiconducting oxides," *J. Phys.: Condens. Matter* **23**, 334212 (2011).
- <sup>36</sup>Y. K. Frodason, C. Zimmermann, E. F. Verhoeven, P. M. Weiser, L. Vines, and J. B. Varley, "Multistability of isolated and hydrogenated Ga–O divacancies in  $\beta$ -Ga<sub>2</sub>O<sub>3</sub>," *Phys. Rev. Mater.* **5**, 025402 (2021).
- <sup>37</sup>M. Kracht, A. Karg, J. Schörmann, M. Weinhold, D. Zink, F. Michel, M. Rohnke, M. Schowalter, B. Gerken, A. Rosenauer *et al.*, "Tin-assisted synthesis of  $\epsilon$ -Ga<sub>2</sub>O<sub>3</sub> by molecular beam epitaxy," *Phys. Rev. Appl.* **8**, 054002 (2017).
- <sup>38</sup>S. M. Sze, Y. Li, and K. K. Ng, *Physics of Semiconductor Devices* (John Wiley & Sons, 2021).
- <sup>39</sup>W. Li, D. Saraswat, Y. Long, K. Nomoto, D. Jena, and H. G. Xing, "Near-ideal reverse leakage current and practical maximum electric field in  $\beta$ -Ga<sub>2</sub>O<sub>3</sub> Schottky barrier diodes," *Appl. Phys. Lett.* **116**, 192101 (2020).
- <sup>40</sup>W. Li, K. Nomoto, D. Jena, and H. G. Xing, "Thermionic emission or tunneling? The universal transition electric field for ideal Schottky reverse leakage current: A case study in  $\beta$ -Ga<sub>2</sub>O<sub>3</sub>," *Appl. Phys. Lett.* **117**, 222104 (2020).